

Chaos of cavity optomechanical system with Coulomb coupling

Yingjia Yang(杨应佳), Liwei Liu(刘利伟), Lianchun Yu(俞连春), Weizheng Kong(孔伟正), Haiyan Jiao(焦海燕), Xiaoyan Deng(邓小燕), and Xiaoyong Li(李小勇)

Citation: Chin. Phys. B, 2025, 34 (**8**): 080503. DOI: 10.1088/1674-1056/add509
http://cpb.iphy.ac.cn; http://iopscience.iop.org/cpb

What follows is a list of articles you may be interested in

Generation of multitype, multicavity chaotic attractors via impulse-function-based state variable extension

Xiaoyu Hu(胡晓宇), Siteng Wang(王思腾), Panpan Wu(邬盼盼), Hongbo Cao(曹红博), Tianwei Yang(杨天纬), and Zhongshuo Dong(董忠硕)

Chin. Phys. B, 2025, 34 (**8**): 080502. DOI: 10.1088/1674-1056/add249

Complexity dynamics analysis of a dual-channel green supply chain with government intervention and cap-and-trade regulation

Yuhao Zhang(张玉豪), Lin Huang(黄林), and Man Yang(杨满)

Chin. Phys. B, 2025, 34 (**7**): 070501. DOI: 10.1088/1674-1056/adca9c

Resonant tunneling diode cellular neural network with memristor coupling and its application in police forensic digital image protection

Fei Yu(余飞), Dan Su(苏丹), Shaoqi He(何邵祁), Yiya Wu(吴亦雅), Shankou Zhang(张善扣), and Huige Yin(尹挥戈)

Chin. Phys. B, 2025, 34 (**5**): 050502. DOI: 10.1088/1674-1056/adb8bb

Model-free prediction of chaotic dynamics with parameter-aware reservoir computing

Jianmin Guo(郭建敏), Yao Du(杜瑶), Haibo Luo(罗海波), Xuan Wang(王晅), Yizhen Yu(于一真), and Xingang Wang(王新刚)

Chin. Phys. B, 2025, 34 (**4**): 040505. DOI: 10.1088/1674-1056/adb733

Nonequilibrium free energy and information flow of a double quantum-dot system with Coulomb coupling

Zhiyuan Lin(林智远), Tong Fu(付彤), Juying Xiao(肖菊英), Shanhe Su(苏山河), Jincan Chen(陈金灿), and Yanchao Zhang(张艳超)

Chin. Phys. B, 2021, 30 (**8**): 080501. DOI: 10.1088/1674-1056/abe119

Chaos of cavity optomechanical system with Coulomb coupling

Yingjia Yang(杨应佳)[1], Liwei Liu(刘利伟)[1,†], Lianchun Yu(俞连春)[2], Weizheng Kong(孔伟正)[1], Haiyan Jiao(焦海燕)[1], Xiaoyan Deng(邓小燕)[1], and Xiaoyong Li(李小勇)[1]

[1] *College of Electrical Engineering, Key Laboratory for Electronic Materials of Northwest Minzu University, Northwest Minzu University, Lanzhou* 730000, *China*

[2] *Lanzhou Center for Theoretical Physics, Key Laboratory of Theoretical Physics of Gansu Province, Key Laboratory of Quantum Theory and Applications of MoE, Gansu Provincial Research Center for Basic Disciplines of Quantum Physics, Lanzhou University, Lanzhou* 730000, *China*

(Received 31 March 2025; revised manuscript received 6 May 2025; accepted manuscript online 7 May 2025)

This study theoretically investigates chaos in a cavity optomechanical system with Coulomb coupling. The system consists of a Fabry–Pérot cavity with a movable mirror, where Coulomb interactions arise from charging the two movable mirrors. We examine the chaotic dynamics under the influence of both single and bichromatic laser fields. The single laser field represents a system driven exclusively by the pump field, whereas the bichromatic field represents simultaneous driving by both the pump and probe fields. In addition to conventional chaos-inducing methods through parameter variations, we demonstrate that increasing the Coulomb coupling strength enhances the system's nonlinearity and induces chaotic behavior. Furthermore, we propose several strategies for generating and controlling chaos, while also identifying the parameter ranges necessary for the resonance of the two mechanical oscillators. Interestingly, when adjusting the driving power in a system driven solely by the pump field, we unexpectedly observe the emergence of high-order sidebands. These findings contribute to the development of chaotic behavior in future cavity optomechanical systems and provide a theoretical basis for applications in physical random number generation and secure communication.

Keywords: cavity optomechanical system, Coulomb coupling, chaos, period bifurcation

PACS: 05.45.–a, 42.50.–p, 42.50.Md, 42.65.Sf

DOI: 10.1088/1674-1056/add509 **CSTR:** 32038.14.CPB.add509

1. Introduction

Optomechanical nonlinearity has emerged as a significant area of research in recent decades.[1–3] As the field continues to advance rapidly, a range of fascinating nonlinear phenomena have been observed in cavity optomechanical systems, including self-induced oscillations,[4–6] tunable high-order sidebands,[7–9] and chaotic motion.[10–12] In addition, cross-Kerr coupling has been demonstrated to significantly impact the transmission spectrum in double-cavity systems.[13] Duffing-type nonlinearities have been utilized to improve quantum entanglement and steering in hybrid atom–optomechanical systems.[14] Nonclassical states have been generated through the use of catalytic quantum scissors,[15] further expanding the domain of optomechanical nonlinearity. The characteristics of chaotic motion are characterized by complex and unpredictable long-term behavior in deterministic dynamical systems, with sensitivity to initial conditions.[16] Experimental studies indicate that increasing the strength of the driving laser can induce chaotic motion in both optical cavities and mechanical oscillators.[17,18] Consequently, considerable attention has been focused on the formation and control of chaotic motion in cavity optomechanical systems.[19,20] In our systems exhibiting nonlinear Coulomb coupling,[21–25] we explore the formation and manipulation of cavity optomechanical chaos through system parameters. This understanding may provide more effective strategies for controlling chaos and offer a novel platform for investigating nonlinear interactions in cavity optomechanics.

Recent advances in nanotechnology have enabled the fabrication of mechanical components with reduced mass and increased quality factors. These improvements significantly strengthen optomechanical interactions. A diverse range of cavity optomechanical systems has been developed, including spherical cavities,[26,27] toroidal oscillators,[28,29] and Fabry–Pérot cavities.[30,31] Introducing additional nonlinearities into these systems not only enriches their dynamics but also unveils new physical phenomena, particularly in the context of chaos. Despite the challenges associated with exploring and controlling chaotic motion, it offers considerable potential for future applications. In quantum optics, Coulomb coupling — achieved by charging a movable mirror — has been employed to observe various nonlinear effects, such as optomechanically induced Faraday rotation,[32] tunable switching between slow and fast light,[33] and superluminal phenomena.[34] Moreover, theoretical studies have demonstrated that Coulomb coupling induces nonlinear interactions within cavity optomechanical systems.[35,36] This offers a promising route for generating and tuning chaotic behavior. In this study, we investigate a Fabry–Pérot cavity with two charged movable mirrors, where Coulomb coupling is deliberately introduced to induce chaos.

[†]Corresponding author. E-mail: liuliw@xbmu.edu.cn

© 2025 Chinese Physical Society and IOP Publishing Ltd. All rights, including for text and data mining, AI training, and similar technologies, are reserved.

In addition to chaotic dynamics, recent advancements in cavity optomechanics have also focused on perfect optomechanically induced transparency, offering new perspectives on light–matter interactions and quantum control.[37,38] These developments further emphasize the importance of exploring the nonlinearity and chaos of cavity optomechanical systems.

This paper aims to improve the controllability of optomechanical chaos by introducing Coulomb coupling. We investigate the system's controllable parameters in both the period-doubling[39,40] and chaotic regimes, considering scenarios with single and bichromatic driving laser fields. By analyzing the radiation–pressure and Coulomb interactions, we explore how various parameters can be adjusted to induce and control chaotic motion under these two interactions. Notably, when only the pump field is present, tunable high-order sideband spectra are observed within the optical cavity, which can be modified by varying the driving power. Numerical simulations of the intracavity field intensity power spectra confirm the presence of high-order sidebands under strong driving conditions. Additionally, we present the bifurcation diagram of the limit cycle amplitude and the corresponding maximum Lyapunov exponent,[41,42] identifying the optimal parameter range that generates chaotic motion. These findings pave the way for further exploration of cavity optomechanical chaos and propose methods for inducing chaos through Coulomb interactions, thereby providing a theoretical foundation for practical applications.

The structure of this paper is as follows: In Section 2, we present the cavity optomechanical model with Coulomb coupling. Using the system's Hamiltonian, we derive the Heisenberg–Langevin equations. In Section 3, we examine the chaotic motion induced by driving power, Coulomb coupling strength, the detuning between the cavity and laser fields, and the detuning the pump and probe fields. We also identify the parameter range for the resonance of the two movable mechanical oscillators. Finally, in Section 4, we summarize the main findings of the paper.

2. Model

The cavity optomechanical system depicted in Fig. 1 consists of a high-quality Fabry–Pérot cavity with an attached movable mechanical oscillator. MR_1 (MR_2) is charged by a bias gate voltage. Mechanical oscillator MR_1 is subjected to both radiation pressure and Coulomb interactions, while mechanical oscillator MR_2 is only influenced by Coulomb interaction. Figure 1(a) illustrates the driving of the pump field, while Fig. 1(b) shows the simultaneous driving of both the pump and probe fields.

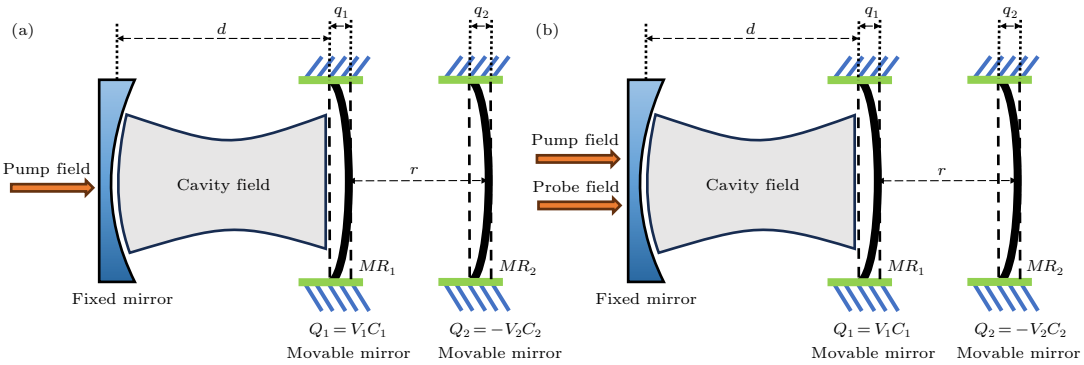


Fig. 1. The schematic diagram of the cavity optomechanical system consisting of an optical cavity and two charged mechanical oscillators, MR_1 and MR_2. The optical cavity has length d. The charges of the oscillators, denoted as Q_1 and Q_2, are $Q_1 = V_1 \cdot C_1$ and $Q_2 = -V_2 \cdot C_2$, respectively. The variables q_1 and q_2 represent the displacements of the oscillators from their equilibrium positions. The equilibrium distance between the two movable mirrors r is also illustrated. (a) A cavity optomechanical system driven only by the pump field. (b) A cavity optomechanical system driven by both the pump and probe fields.

First, we examine the case of a single driving laser with only a pump field. The Hamiltonian of the system is expressed as

$$H_1 = \hbar\omega_c c^\dagger c - \hbar g c^\dagger c q_1 + \hbar\lambda q_1 q_2 + \mathrm{i}\hbar\Omega_l (c^\dagger \mathrm{e}^{-\mathrm{i}\omega_l t} - \mathrm{H.c.}) + \left(\frac{p_1^2}{2m_1} + \frac{1}{2}m_1\omega_1^2 q_1^2\right) + \left(\frac{p_2^2}{2m_2} + \frac{1}{2}m_2\omega_2^2 q_2^2\right). \quad (1)$$

The first term of the Hamiltonian corresponds to the energy of an optical cavity field with frequency ω_c, where c ($c^\dagger$) is the annihilation (creation) operator of the optical cavity field, respectively. MR_1 and MR_2 represent movable mirrors with effective masses m_1 and m_2, respectively. The parameters $g = \omega_c/d$ and $\lambda = C_1V_1C_2V_2/(2\pi\hbar\varepsilon_0 r^3)$ denote the coupling strengths of the optical cavity field and Coulomb interaction,[43,44] where d is the length of the Fabry–Pérot cavity and ε_0 is the vacuum dielectric constant. C_1 (C_2) and V_1 (V_2) represent the bias capacitance and bias voltage, respectively, where charge and discharge operations are applied to the movable mirror. The second term corresponds to the interaction Hamiltonian of MR_1 coupled to the cavity field via radiation pressure. The third term accounts for the Coulomb interaction between MR_1 and MR_2. The fourth term corresponds to

the Hamiltonian of the pump field, where $\Omega_{\rm l}=\sqrt{2\kappa P_{\rm l}/\hbar\omega_{\rm l}}$ is the amplitude, which is related to the field's power $P_{\rm l}$. Here, $P_{\rm l}$ represents the power of the field and κ is the total loss rate of the optical cavity field. The final two terms describe the free Hamiltonians governing the oscillations of the two movable mirrors MR_1 (MR_2) with ω_1 (ω_2), q_1 (q_2) and p_1 (p_2) representing the frequency, position and momentum of the mirrors, respectively. Finally, under the rotating frame defined by the driving laser frequency $\omega_{\rm l}$ of the pump laser, the Hamiltonian is rewritten as follows:

$$\begin{aligned}H_1' =\ & \hbar\Delta_{\rm c}c^{\dagger}c-\hbar g c^{\dagger}cq_1+\hbar\lambda q_1q_2+{\rm i}\hbar\Omega_{\rm l}(c^{\dagger}-c)\\ &+\left(\frac{p_1^2}{2m_1}+\frac{1}{2}m_1\omega_1^2q_1^2\right)+\left(\frac{p_2^2}{2m_2}+\frac{1}{2}m_2\omega_2^2q_2^2\right),\end{aligned}\tag{2}$$

where $\Delta_{\rm c}=\omega_{\rm c}-\omega_{\rm l}$ is the detuning of cavity field frequency and pump field frequency.

The cavity optomechanical system exhibits strong nonlinear behavior, resulting in complex dynamics, including chaos. Although the system operates in a relatively strong optomechanical coupling regime, we adopt the mean-field approximation to study the nonlinear dynamical behavior. It should be noted that, in principle, the mean-field approximation $\langle Qa\rangle=\langle Q\rangle\langle a\rangle$ is more appropriate for systems operating in the single-photon weak-coupling regime.[45] Here, it is employed primarily to qualitatively capture the nonlinear features, as demonstrated in Refs. [33,43,46]. The dynamics of the system can be described by the Heisenberg–Langevin equations,[47] which accurately capture the complex phenomena induced by nonlinear terms. To facilitate a discussion of the nonlinear and chaotic dynamics of the system, we define the average value of the optical cavity field $c=c_{\rm re}+{\rm i}c_{\rm im}$, where $c_{\rm re}$ and $c_{\rm im}$ represent the real and imaginary numbers, respectively. Finally, the semiclassical equations of motion, free of imaginary terms, are given as

$$\dot{q}_1=\frac{p_1}{m_1},\tag{3a}$$

$$\dot{p}_1=\hbar g(c_{\rm re}^2+c_{\rm im}^2)-m_1\omega_1^2q_1-\hbar\lambda q_2-\gamma_1p_1,\tag{3b}$$

$$\dot{q}_2=\frac{p_2}{m_2},\tag{3c}$$

$$\dot{p}_2=-m_2\omega_2^2q_2-\hbar\lambda q_1-\gamma_2p_2,\tag{3d}$$

$$\dot{c}_{\rm re}=-\kappa c_{\rm re}+(\Delta_{\rm c}-gq_1)c_{\rm im}+\Omega_{\rm l},\tag{3e}$$

$$\dot{c}_{\rm im}=-\kappa c_{\rm im}-(\Delta_{\rm c}-gq_1)c_{\rm re}.\tag{3f}$$

Here, the decay rate of the optical cavity field is denoted by κ, while γ_1 and γ_2 represent the loss rates of the two movable mirrors, respectively.

The system is simultaneously driven by both the pump field and the probe field. In the rotating frame with respect to the pump field frequency $\omega_{\rm l}$, the effective Hamiltonian is given by

$$\begin{aligned}H_2 =\ & \hbar\Delta_{\rm c}c^{\dagger}c-\hbar g c^{\dagger}cq_1+\hbar\lambda q_1q_2+\left(\frac{p_1^2}{2m_1}+\frac{1}{2}m_1\omega_1^2q_1^2\right)\\ &+\left(\frac{p_2^2}{2m_2}+\frac{1}{2}m_2\omega_2^2q_2^2\right)+{\rm i}\hbar\Omega_{\rm l}(c^{\dagger}-c)\\ &+{\rm i}\hbar(c^{\dagger}\Omega_{\rm s}\,{\rm e}^{-{\rm i}\Delta_{\rm sl}t}-{\rm H.c.}).\end{aligned}\tag{4}$$

Here, $\Delta_{\rm sl}=\omega_{\rm s}-\omega_{\rm l}$ is the detuning between the probe and pump field frequencies. $\Omega_{\rm s}=\sqrt{2\kappa P_{\rm s}/\hbar\omega_{\rm s}}$ is the amplitude of the probe field, which is related to the field's power $P_{\rm s}$. Similarly, the semiclassical Heisenberg–Langevin equations are presented to describe the motion of the system

$$\dot{q}_1=\frac{p_1}{m_1},\tag{5a}$$

$$\dot{p}_1=\hbar g(c_{\rm re}^2+c_{\rm im}^2)-m_1\omega_1^2q_1-\hbar\lambda q_2-\gamma_1p_1,\tag{5b}$$

$$\dot{q}_2=\frac{p_2}{m_2},\tag{5c}$$

$$\dot{p}_2=-m_2\omega_2^2q_2-\hbar\lambda q_1-\gamma_2p_2,\tag{5d}$$

$$\dot{c}_{\rm re}=-\kappa c_{\rm re}+(\Delta_{\rm c}-gq_1)c_{\rm im}+\Omega_{\rm l}+\Omega_{\rm s}\cos(\Delta_{\rm sl}t),\tag{5e}$$

$$\dot{c}_{\rm im}=-\kappa c_{\rm im}-(\Delta_{\rm c}-gq_1)c_{\rm re}-\Omega_{\rm s}\sin(\Delta_{\rm sl}t),\tag{5f}$$

The quadratic $[\hbar g(c_{\rm re}^2+c_{\rm im}^2)]$ and mixed terms $[-gq_1c_{\rm im}$ and $-gq_1c_{\rm re}]$ in the Heisenberg–Langevin equation demonstrate the system's nonlinearity. Chaotic motion is highly sensitive to initial conditions. We introduce the system's perturbation equations $\varepsilon_0=(\varepsilon_{q_1},\varepsilon_{p_1},\varepsilon_{q_2},\varepsilon_{p_2},\varepsilon_{c_{\rm re}},\varepsilon_{c_{\rm im}})$ to characterize this chaotic behavior. The chaotic motion can be assessed by calculating the average exponential divergence rate between two adjacent trajectories.

$$\dot{\varepsilon}_{q_1}=\frac{\varepsilon_{p_1}}{m_1},\tag{6a}$$

$$\dot{\varepsilon}_{p_1}=2\hbar g(\varepsilon_{c_{\rm re}}c_{\rm re}+\varepsilon_{c_{\rm im}}c_{\rm im})-m_1\omega_1^2\varepsilon_{q_1}-\hbar\lambda\varepsilon_{q_2}-\gamma_1\varepsilon_{p_1},\tag{6b}$$

$$\dot{\varepsilon}_{q_2}=\frac{\varepsilon_{p_2}}{m_2},\tag{6c}$$

$$\dot{\varepsilon}_{p_2}=-m_2\omega_2^2\varepsilon_{q_2}-\hbar\lambda\varepsilon_{q_1}-\gamma_2\varepsilon_{p_2},\tag{6d}$$

$$\dot{\varepsilon}_{c_{\rm re}}=-\kappa\varepsilon_{c_{\rm re}}-g(c_{\rm im}\varepsilon_{q_1}+\varepsilon_{c_{\rm im}}q_1)+\Delta_{\rm c}\varepsilon_{c_{\rm im}},\tag{6e}$$

$$\dot{\varepsilon}_{c_{\rm im}}=-\kappa\varepsilon_{c_{\rm im}}-\Delta_{\rm c}\varepsilon_{c_{\rm re}}+g(q_1\varepsilon_{c_{\rm re}}+c_{\rm re}\varepsilon_{q_1}).\tag{6f}$$

Furthermore, we introduce the maximum Lyapunov exponent, denoted as $\mathrm{LE}_{\max}$. It is characterized by the logarithmic slope of the perturbation's evolution ε_0 as time approaches infinity, providing a description of the state of optical cavities or mechanical oscillators,[11,48]

$$\mathrm{LE}_{\max}=\lim_{t\to\infty}\lim_{\delta q_0\to0}\frac{1}{t}\ln\left(\frac{|\delta q(t)|}{|\delta q_0|}\right).\tag{7}$$

When $\mathrm{LE}_{\max}>0$, the system exhibits chaotic behavior, with small errors being exponentially amplified, leading to significant divergences between adjacent trajectories. Conversely,

when $\mathrm{LE}_{\max} < 0$, the system is stable, and adjacent trajectories converge to a steady state. When $\mathrm{LE}_{\max} = 0$, the system is in a critical state, transitioning between chaos, periodic motion, and period-doubling.

3. Results and discussion

In this study, we extend the classical Fabry–Pérot cavity by incorporating a movable mechanical resonator and introducing Coulomb coupling between the two resonators. Our focus is on investigating the effects of the driving laser field, detuning and Coulomb coupling strength on the cavity optomechanical system.

In our exploration of the system's nonlinearity, driven by a single laser field, we first observed the generation of tunable higher-order sidebands as the laser power increased, as illustrated in Figs. 2(a)–2(d).

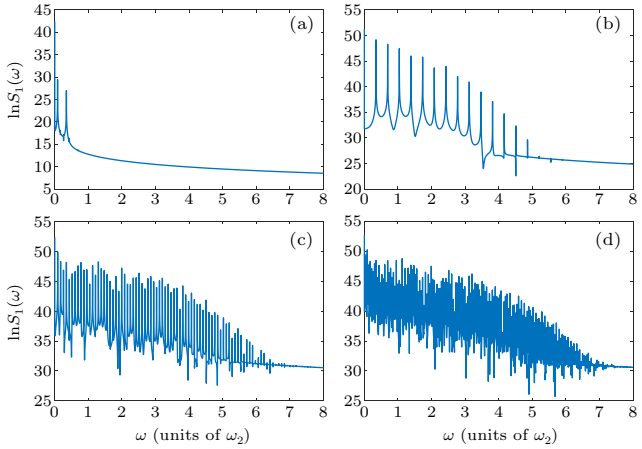


Fig. 2. Logarithmic power spectra corresponding to various pump field powers P_l: (a) $P_l = 0.2$ mW, (b) $P_l = 20$ mW, (c) $P_l = 60$ mW and (d) $P_l = 100$ mW. The remaining parameters are as follows: $d = 25$ mm, $\lambda_l = 1064$ nm, $m_1 = m_2 = 145$ ng, $\omega_l = 2\pi \times 947 \times 10^3$ Hz, $\omega_2 = 1/2\omega_1$, $Q_1 = Q_2 = 6700$, $\kappa = 2\pi \times 215 \times 10^3$ Hz, $\Delta_c = \omega_c - \omega_l = -1.5\omega_2$, and $\lambda = 2 \times 10^{37}$ Hz$\cdot$m^{-2}.

By numerically solving the system, we define $I_c = c_{re}^2 + c_{im}^2$, which corresponds to the intracavity field intensity. As shown in Fig. 2, with an increase in the pump field power P_l, the sidebands within the optical cavity expand significantly. The power spectra are plotted based on the Fourier transform for different pump field powers: $P_l = 0.2$ mW; $P_l = 20$ mW; $P_l = 60$ mW; $P_l = 100$ mW. In Fig. 2(a), for weak pump field power $P_l = 0.2$ mW, only low-order sidebands, such as the first and second-order sidebands, are induced. In Fig. 2(b), when pump field power increases to $P_l = 20$ mW, higher-order sidebands appear within the optical cavity, showing a gradual decrease in the power spectra. Further increases in pump field power to $P_l = 60$ mW and $P_l = 100$ mW lead to the generation of additional higher-order sidebands, as seen in Figs. 2(c) and 2(d). It is evident that as the pump field power increases, the number of higher-order sidebands also increases within the optical cavity. During this process, the strength of each higher-order sideband progressively weakens, eventually resulting in a sharp cutoff. This behavior is indicative of robust high-order sideband generation (HSG). Furthermore, in Figs. 2(c) and 2(d), the HSG in the optical cavity becomes denser with increasing pump field power, highlighting the enhancement of nonlinear effects in the system due to the increased pump field power.

We now focus on the evolution of position q_1 (q_2) and the phase space of q_1 (q_2) and p_1 (p_2) under the influence of Coulomb interaction between the two mechanical oscillators, as shown in Fig. 3. As the Coulomb coupling strength increases, the motion of the two oscillators alternates between chaotic and periodic regimes, demonstrating the system's high sensitivity to Coulomb interaction. When Coulomb coupling strength is below a critical threshold, as illustrated in Figs. 3(a), 3(e), 3(i) and 3(m), both mechanical oscillators exhibit periodic motion, forming closed curves in phase space, which corresponds to a single-period limit cycle. As the Coulomb coupling strength increases, the oscillators transition from periodic motion to chaotic motion, as seen in Figs. 3(b), 3(f), 3(j) and 3(n). During chaotic motion, the system does not return to the same state, continuously evolving into new states due to its sensitivity to initial conditions. A small change in initial conditions can lead to a divergence in the system's evolution, resulting in distinct trajectories. Continuing to increase λ, the oscillator returns to periodic motion, as shown in Figs. 3(c), 3(g), 3(k) and 3(o). However, as shown in Figs. 3(d), 3(h), 3(l) and 3(p), chaotic motion reappears at higher Coulomb coupling strength. After alternating between ordered and disordered states, the system eventually enters a permanent chaotic state. This behavior contrasts with the typical branching paths observed at lower coupling strengths. As the Coulomb coupling increases, the optomechanical nonlinear effects intensify, contributing to system instability. By comparing the motion and trajectories of two mechanical oscillators, MR_1 and MR_2, under identical conditions, it can be observed that both oscillators share the same state, such as periodic motion, period-doubling bifurcation, or chaos. This similarity can be attributed to the Coulomb interaction between the oscillators. As the Coulomb coupling strength λ is varied, the states of the two oscillators change accordingly. By modifying the Coulomb coupling strength λ, we can induce chaotic motion in the mechanical oscillator. This demonstrates that the Coulomb coupling strength becomes the determining factor in the motion state of the mechanical oscillators.

To determine the parameter range for chaotic motion induced by Coulomb interaction, we plotted bifurcation diagrams and the corresponding $\mathrm{LE}_{\max}$ for MR_1 and MR_2. As shown in Figs. 4(a) and 4(b), the bifurcation diagrams illustrate the variation in the limit cycle amplitude of the oscillators' mechanical motion MR_1 and MR_2 with Coulomb coupling strength λ. The bifurcation diagrams clearly depict the

oscillators alternating between periodic and chaotic motion, eventually reaching permanent chaos. Figures 4(c) and 4(d) show the variation of the LE_{max} for the two oscillators with Coulomb coupling strength λ. These curves also reveal the alternating transition between periodic and chaotic motion, ultimately leading to permanent chaos. The maximum Lyapunov exponent quantifies the sensitivity of the oscillators to initial conditions, displaying alternating positive and negative values. In the cavity optomechanical system driven solely by the pump field, we also identified the optimal Coulomb coupling range for resonance between the oscillators. Within this range, the oscillators become tightly coupled via Coulomb interaction, enhancing the nonlinear effects and allowing both oscillators to reach chaotic states simultaneously.

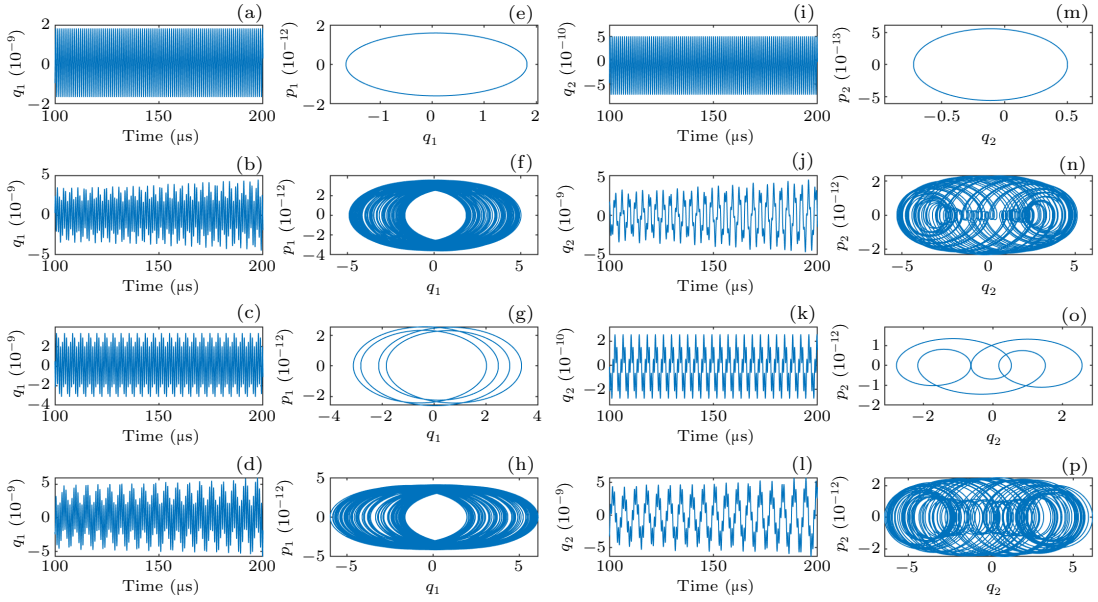


Fig. 3. Panels (a)–(d) show the evolution of q_1, while panels (e)–(h) present the phase space of q_1 and p_1 of MR_1. Panels (i)–(l) depict the evolution of q_2, and panels (m)–(p) display the phase space of q_2 and p_2 of MR_2. The values of the Coulomb coupling strength λ are listed from top to bottom as 1.5×10^{37} Hz$\cdot$m^{-2}, 1.78×10^{37} Hz$\cdot$m^{-2}, 2.0×10^{37} Hz$\cdot$m^{-2} and 2.2×10^{37} Hz$\cdot$m^{-2}. Here $P_l = 60$ mW, $\Delta_c = -1.5\omega_2$, all other parameters are the same as those in Fig. 2.

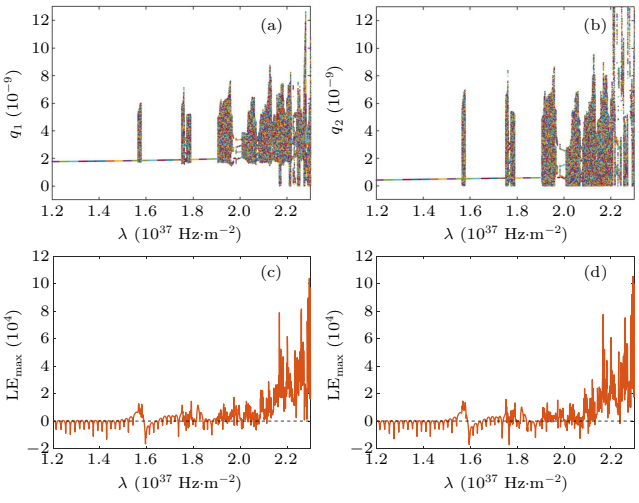


Fig. 4. (a) Bifurcation diagram of mechanical oscillator MR_1. (b) Bifurcation diagram of mechanical oscillator MR_2. (c) LE_{max} of mechanical oscillator MR_1. (d) LE_{max} of mechanical oscillator MR_2 under varying Coulomb coupling strength λ. All other parameters are identical to those in Fig. 3.

Furthermore, we observed the transition from periodic motion to chaos by adjusting the detuning between the pump field and the optical cavity. Figures 5(a)–5(d) show that as the detuning Δ_c increases, both the amplitude and frequency of the oscillations change. Specifically, when the detuning $\Delta_c = 0.3\omega_2$ and $\Delta_c = 0.9\omega_2$ as illustrated in Figs. 5(a) and 5(b), variation of the intracavity field intensity I_c shows periodic motion. However, as the detuning Δ_c increases, the system's nonlinear behavior gradually shifts from periodic oscillations to chaotic motion. As shown in Fig. 5(c), at a specific detuning value $\Delta_c = 1.4\omega_2$, the optical cavity enters a chaotic state, displaying irregular and unpredictable dynamics. With further increases in detuning $\Delta_c = 1.8\omega_2$, as shown in Fig. 5(d), the system gradually stabilizes and the optical cavity approaches a steady value. To investigate the nonlinear dynamics of two mechanical oscillators in an optomechanical cavity system with varying detuning values Δ_c, we analyzed the evolution of the oscillators. Figures 5(e)–5(l) illustrate the dynamics of the oscillators MR_1 and MR_2 as a function of detuning Δ_c. Initially, we focus on the evolution of mechanical oscillator MR_1 in terms of its position q_1. At specific detuning values $\Delta_c = 0.3\omega_2$ and $0.9\omega_2$, mechanical oscillator MR_1 exhibits periodic motion, as shown in Figs. 5(e) and 5(f). At certain detuning $\Delta_c = 1.4\omega_2$, as depicted in Fig. 5(g), mechanical oscillator MR_1 transitions into chaotic motion. As detuning continues to increase $\Delta_c = 1.8\omega_2$, as shown in Fig. 5(h), oscillator MR_1 stabilizes, approaching a steady state. Next, we examine the evolution of the second mechanical oscillator under the same detuning conditions. Figures 5(i) and 5(j) show resonance phenomena within a specific parameter range,

where both oscillators MR_2 and MR_1 undergo periodic oscillations simultaneously. Similarly, in Fig. 5(k), MR_2 enters a chaotic state at higher detuning values $\Delta_c = 1.4\omega_2$. As detuning continues to increase $\Delta_c = 1.8\omega_2$, the amplitudes of oscillator MR_2 gradually decrease, eventually reaching a stable and fixed value. Under these conditions, the two mechanical oscillators and the optical cavity synchronize, either exhibiting periodic or chaotic motion in unison.

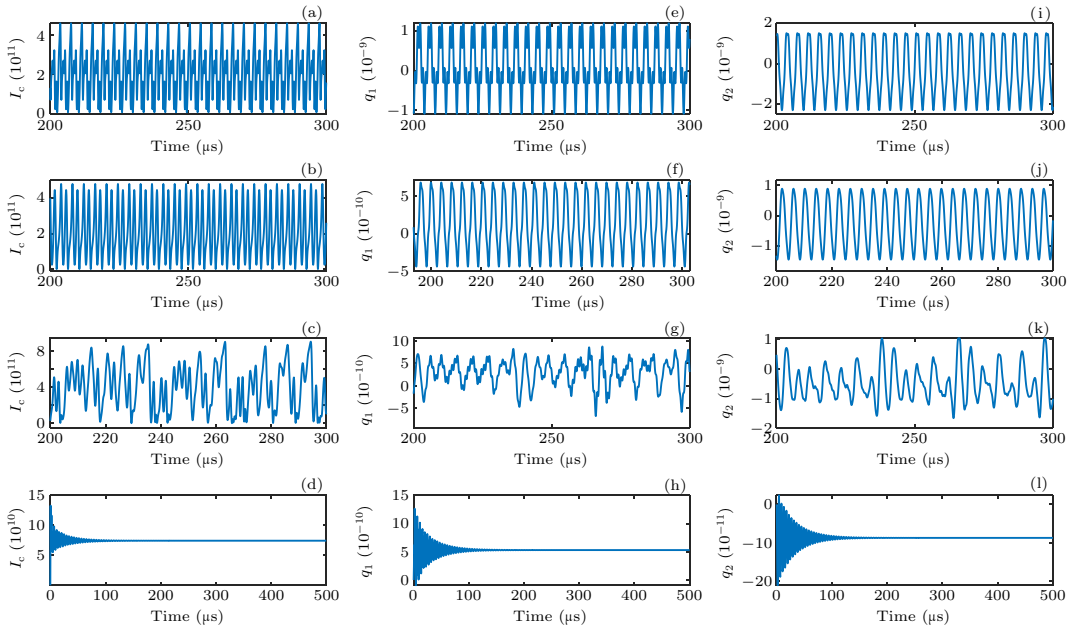


Fig. 5. Panels (a)–(d) show the evolution of the intracavity field intensity I_c. Panels (e)–(h) depict the evolution of position q_1 of mechanical oscillator MR_1, while panels (i)–(l) illustrate the evolution of position q_2 of mechanical oscillator MR_2. The values of the detuning Δ_c are $0.3\omega_2$,$0.9\omega_2$, $1.4\omega_2$ and $1.8\omega_2$ from top to bottom. All other parameters remain consistent with those in Fig. 2.

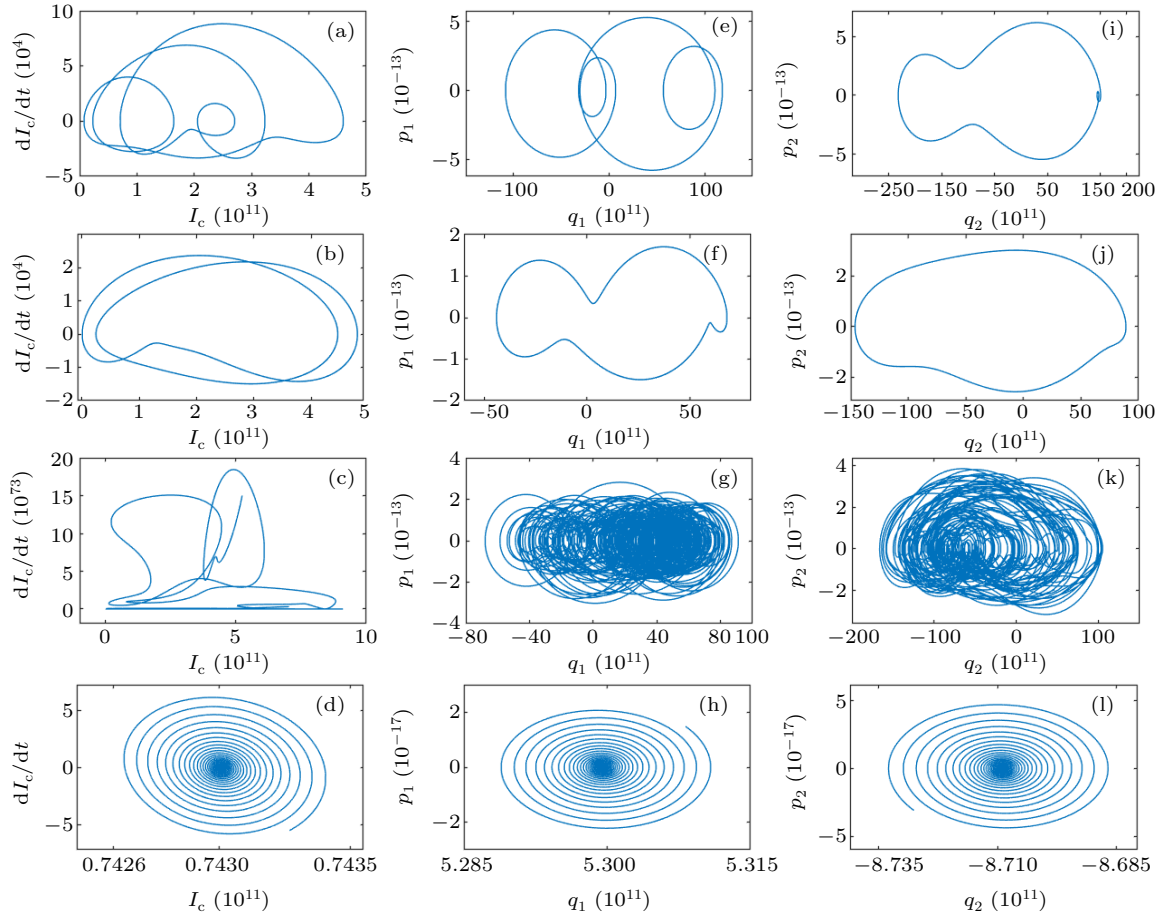


Fig. 6. The phase space of the system as the detuning Δ_c between the pump field and the optical cavity changes, the values of the detuning Δ_c are $0.3\omega_2$, $0.9\omega_2$, $1.4\omega_2$ and $1.8\omega_2$ from top to bottom. Panels (a)–(d) depict the phase space of the optical cavity, (e)–(h) represent the phase space of mechanical oscillator MR_1, and (i)–(l) show the phase space of mechanical oscillator MR_2. Other parameters remain the same as those in Fig. 2.

The system's evolution reveals that chaos can be induced by adjusting the detuning Δ_c. The relationship between the system's phase space and the detuning Δ_c is illustrated in Fig. 6. Specifically, figures 6(a) and 6(b) show the phase space of the optical cavity as a function of the detuning parameters $\Delta_c = 0.3\omega_2$ and $\Delta_c = 0.6\omega_2$. When the detuning is small, the trajectories form simple closed curves, indicating periodic motion of the cavity field. Under the same conditions, the phase space of mechanical oscillators MR_1 and MR_2, as shown in Figs. 6(e), 6(f), 6(i) and 6(j), also exhibits stable and regular trajectories. As the detuning $\Delta_c = 1.4\omega_2$ exceeds a certain threshold, the system's trajectories become increasingly complex, with the optical cavity and the two mechanical oscillators beginning to exhibit chaotic behavior. In Figs. 6(c), 6(g) and 6(k), the trajectories shift from closed curves to irregular, unpredictable paths. In the chaotic regime, the interaction between the optical cavity and the mechanical oscillators amplifies the complexity and sensitivity of the phase space, causing small changes in initial conditions to result in significant bifurcations. As the detuning continues to increase $\Delta_c = 1.9\omega_2$, as shown in Figs. 6(d), 6(h), and 6(l), the trajectories eventually converge to a point and the system stabilizes in a stable attractor. In this state, all trajectories converge to the attractor, indicating that the system's evolution approaches a steady state. This further illustrates the transition from chaotic nonlinear behavior to a steady state as the detuning increases.

After analyzing the case of a single driving laser field, we will next examine the bichromatic laser field, consisting of both a pump field and a probe field. We will then explore the formation and manipulation of chaos, focusing on the effects of the probe field's driving power, Coulomb coupling strength and the detuning between the two laser fields.

Firstly, figures 7(a)–7(e) illustrate the gradual transition of mechanical oscillator MR_1 from periodic to chaotic motion as the probe field power increases. In Fig. 7(a), when the probe field is absent, the evolution of position q_1 of oscillator MR_1 exhibits smooth periodic motion. This occurs because the system is primarily driven by the pump field and the lack of the probe field reduces coherent effects and interference, causing the periodic motion to resemble a sine function $x(t) = x_0 + A\cos(\Omega t)$. Comparing Figs. 7(a) and 7(b), as the probe field power increases form $P_s = 0$ mW to $P_s = 9$ mW, the amplitude of position q_1 increases and a period-doubling bifurcation occurs. In Fig. 7(c), when the probe field $P_s = 12$ mW is applied, the oscillator's behavior becomes unpredictable, indicating a transition to a chaotic state. In Fig. 7(d), as the probe field power further increases to $P_s = 16$ mW, oscillator MR_1 undergoes another period-doubling bifurcation. In Fig. 7(e), when the probe field power reaches $P_s = 18$ mW, MR_1 has fully transitioned to a chaotic state. This represents a classic route from period-doubling bifurcation to chaos.

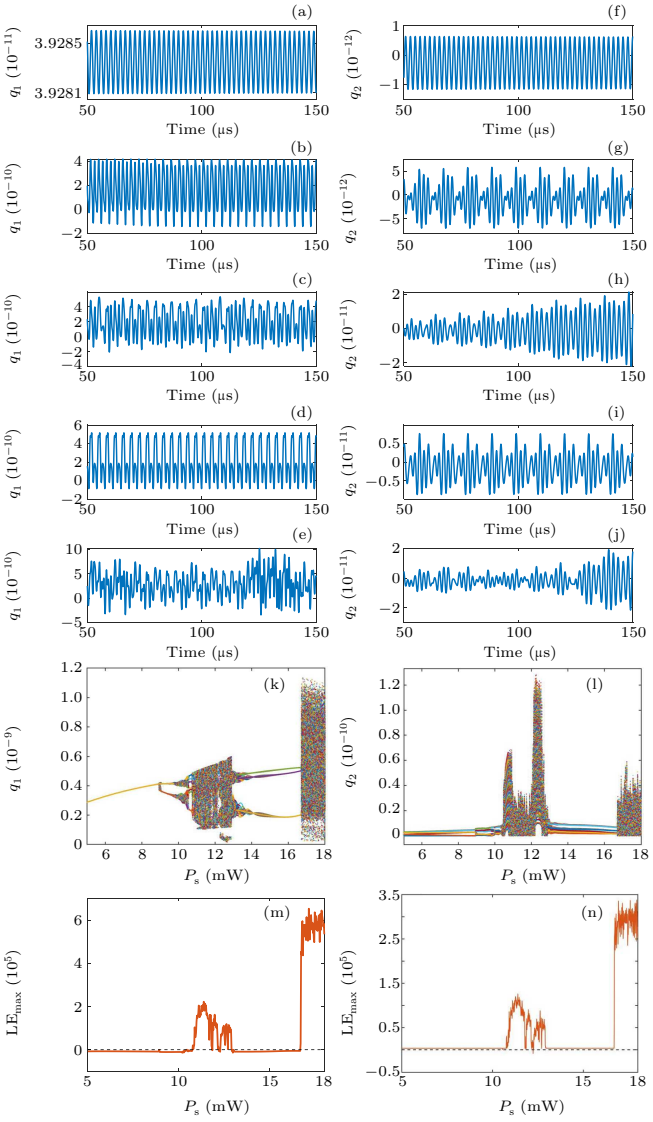


Fig. 7. (a)–(e) The evolution of position q_1 at different probe field powers P_s. (f)–(j) The evolution of position q_2 at different probe field powers P_s. (k), (l) Bifurcation diagram of the limit cycle amplitude for mechanical oscillators MR_1 and MR_2 as a function of probe field power P_s. (m), (n) Maximum Lyapunov exponent (LE_{max}) for mechanical oscillators MR_1 and MR_2 and the probe field power P_s. The probe field powers are denoted by $P_s = 0$ mW, $P_s = 9$ mW, $P_s = 12$ mW, $P_s = 16$ mW and $P_s = 18$ mW, respectively. Other parameters remain the same as those in Fig. 2.

Figures 7(f)–7(j) depict the evolution of another mechanical oscillator MR_2. In Fig. 7(f), the motion of MR_2 can also be described by a sine function, as the system is driven by a single laser field with fixed frequency and amplitude, and no additional driving forces or perturbations are present. Under these conditions, the oscillator exhibits periodic, regular harmonic oscillations. After introducing the probe field $P_s = 9$ mW, as shown in Fig. 7(g), the motion of MR_2 remains periodic, but symmetry emerges, reflecting strong energy exchange between the oscillators. As the probe field power increases to $P_s = 12$ mW, as shown in Fig. 7(h), this symmetry gradually breaks down, resulting in symmetry-breaking chaos.[49,50] Figures 7(i) and 7(j) show that as the probe field power increases from $P_s = 16$ mW to $P_s = 18$ mW, the system transi-

tions from periodic motion to symmetry-breaking chaos once again. Comparing the evolution of MR_1 and MR_2, it is evident that under the given conditions, both oscillators exhibit simultaneous periodic and chaotic behavior as the probe field power changes.

Secondly, the evolution of position q_1 and q_2 clearly demonstrates its nonlinear dynamical behavior under fixed conditions. Figures 7(k)–7(n) illustrate the state changes of MR_1 and MR_2 at various probe field powers. Figures 7(k) and 7(l) provide a more detailed depiction of the route to chaos by showing bifurcation diagrams of the system's amplitudes of positions q_1 and q_2 as the probe field power P_s changes. This transition to chaos is observed as the input power of the probe field varies. Additionally, $\mathrm{LE_{max}}$ is calculated to distinguish between the periodic and chaotic motion of the mechanical oscillators, as shown in Figs. 7(m) and 7(n). At low probe field power $P_s < 8.93$ mW, MR_1, and MR_2 exhibit stable periodic motion. As the power $P_s > 8.93$ mW, the motion of the mechanical oscillator begins to exhibit period-doubling bifurcation. It can be seen from the bifurcation diagram and $\mathrm{LE_{max}}$ that the system has entered a period of chaos when $12.90\ \mathrm{mW} > P_s > 8.93\ \mathrm{mW}$. Afterwards, the system returned to periodic motion. Finally, after $P_s > 16.70$ mW, the motion of the mechanical oscillator entered large-scale chaos.

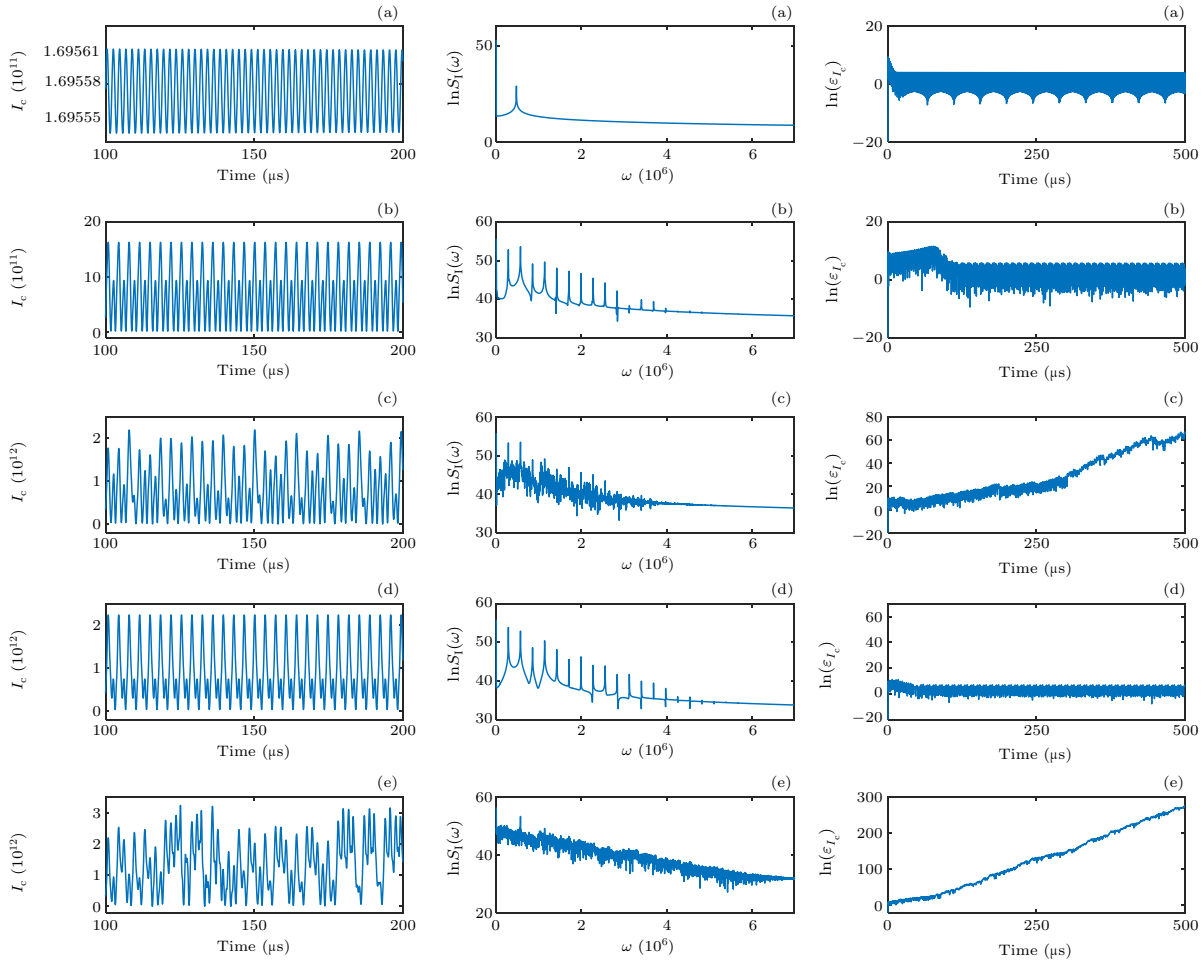


Fig. 8. (a)–(e) The evolution of the intracavity field intensity I_c, (f)–(j) the power spectral density curves and (k)–(o) the logarithmic perturbation $\ln(\varepsilon_{I_c})$ at different probe field powers P_s. The values of P_s are 0 mW, 9 mW, 12 mW, 16 mW and 18 mW from top to bottom, respectively. All other parameters are the same as those in Fig. 7.

Furthermore, figures 8(a)–8(o) illustrate the evolution of the intracavity field intensity I_c, logarithmic power spectral density $\ln S_I(\omega)$ and logarithmic perturbation $\ln(\varepsilon_{I_c})$ as a function of the probe field power P_s. In Figs. 8(a), 8(f) and 8(k), when the probe field power is absent $P_s = 0$ mW, the signal is a pure sine wave and the spectrum consists of single-frequency component without higher-order sidebands. However, in Figs. 8(b), 8(g) and 8(l), as the probe field power increases $P_s = 9$ mW, period-doubling bifurcation occurs in the optical cavity's evolution, and higher-order sidebands appear in the signal due to enhanced nonlinear effects induced by the probe field. With further increases in power $P_s = 12$ mW, as shown in Figs. 8(c), 8(h) and 8(m), the optical cavity transitions into a chaotic state, and the power spectrum becomes continuous, exhibiting noise characteristics that confirm the onset of chaos. At an even higher power level $P_s = 16$ mW, as shown in Figs. 8(d), 8(i) and 8(n), the optical cavity shifts from chaos back to periodic motion, and the power spectrum transitions from a continuous to a discrete state. The evolution of the perturbation returns to a flat state, indicating the

disappearance of chaotic motion. When the probe field power reaches even higher levels $P_s = 18$ mW, as shown in Figs. 8(e), 8(j) and 8(o), the optical cavity again enters a chaotic state. Furthermore, comparing the evolution of the perturbations in chaotic states, it is evident that the slope in Fig. 8(o) is steeper than that in Fig. 8(m), indicating that as the probe field power increases, the degree of chaos in the system intensifies. In contrast, the evolution of the remaining perturbations remains stable, as shown in Figs. 8(k), 8(l) and 8(n), suggesting that the system at this point is not affected by minor changes in initial conditions. Finally, under our conditions, the comparison between Figs. 7 and 8 reveals that the optical cavity field and the two mechanical oscillators enter or exit chaos simultaneously.

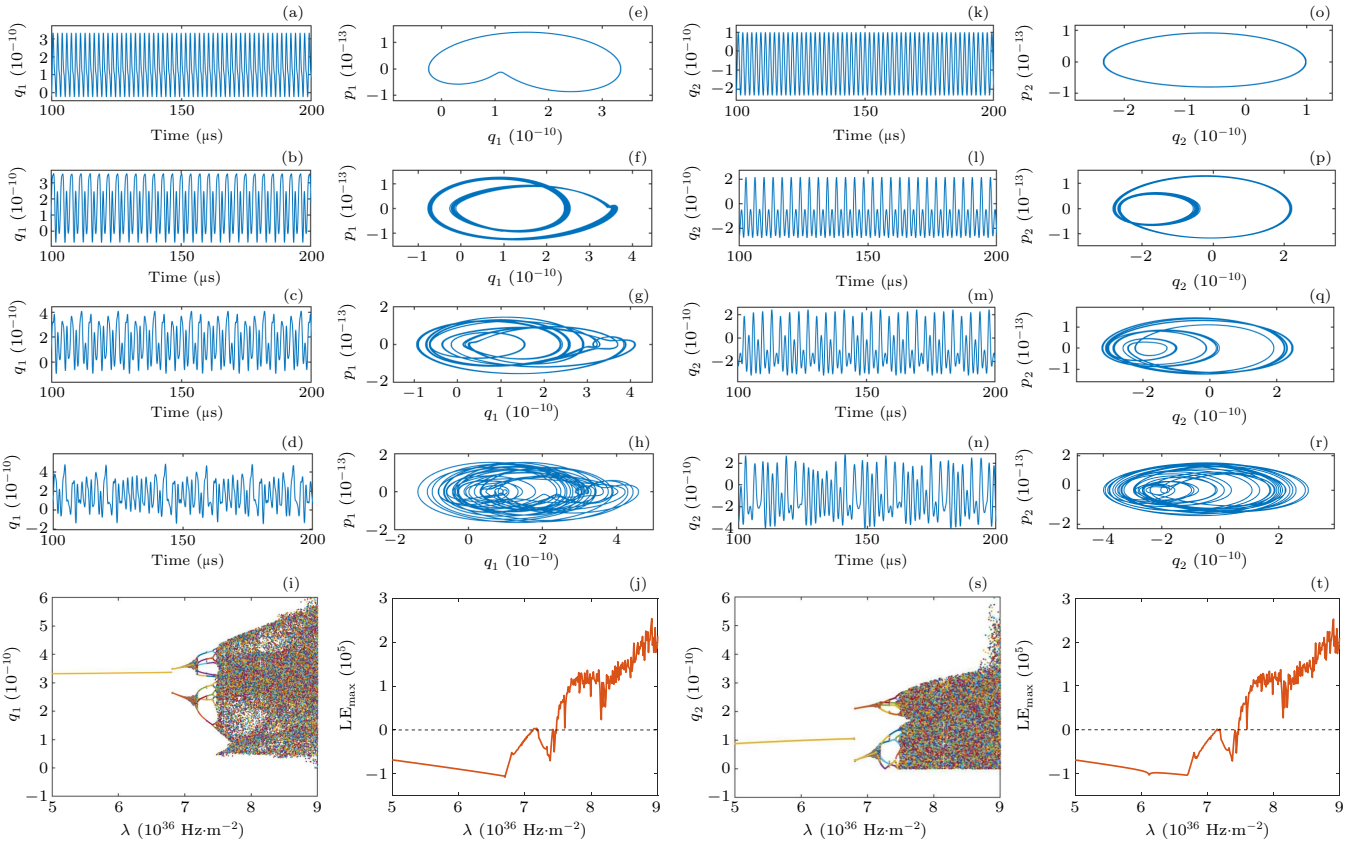


Fig. 9. Panels (a)–(h) and (k)–(r) depict the evolution of the position and phase space of the mechanical oscillators for varying Coulomb coupling strength λ. The values of λ from top to bottom are 6×10^{36} Hz$\cdot$m^{-2}, 7×10^{36} Hz$\cdot$m^{-2}, 7.4×10^{36} Hz$\cdot$m^{-2} and 8×10^{36} Hz$\cdot$m^{-2}. Panels (i) and (s) show bifurcation diagrams of the limit cycle amplitude of mechanical oscillators MR_1 and MR_2 as a function of Coulomb coupling strength λ, respectively. Panels (j) and (t) present the maximum Lyapunov exponent (LE$_{max}$) of mechanical oscillators MR_1 and MR_2 as a function of λ. Except for the specified variables, all other parameters are identical to those in Fig. 7.

In the following, we investigate the chaotic dynamics induced by Coulomb interactions. The evolution of the position and phase space of the mechanical oscillators for varying Coulomb coupling strengthλ are illustrated in Figs. 9(a)–9(h) and 9(k)–9(r). Once the Coulomb coupling strength λ reaches a certain threshold, mechanical oscillators MR_1 and MR_2 enter a chaotic state. Figures 9(a) and 9(k) show that the positions of the two mechanical oscillators exhibit periodic motion within one cycle, and periodic trajectories in phase space, as depicted in Figs. 9(e) and 9(o). These trajectories, resembling ellipses, correspond to the temporal evolution of the system. When the Coulomb coupling strength $\lambda = 7\times10^{36}$ Hz$\cdot$m^{-2} is below a critical value, the oscillators remain in periodic oscillation, as expected from previous analysis. In contrast, figures 9(b) and 9(l) reveal that increasing the Coulomb coupling strength triggers period-doubling behavior, evident in both the temporal evolution and phase space, as shown in Figs. 9(f) and 9(p), which display two closed trajectories. By increasing the Coulomb coupling strength, figures 9(c) and 9(m) illustrate further period-doubling behavior, with the phase space showing multiple attractors that gradually evolve toward a disordered state, as seen in Figs. 9(g) and 9(q). As the Coulomb coupling strength continues to increase $\lambda = 8\times10^{36}$ Hz$\cdot$m^{-2}, figures 9(d) and 9(n) show that the time-domain signals become increasingly erratic, while the phase-space trajectories become complex and non-repetitive, as depicted in Figs. 9(h) and 9(r), this confirms that the system has entered a fully chaotic state. The phase-space diagrams further highlight the impact of Coulomb coupling strength: as λ increases, the system transitions from period-doubling to chaotic motion. As shown in Eqs. (5a)–(5f), the terms involving λ in the mechanical oscillator are linear. The sources of nonlinearity in the

system are primarily quadratic [$\hbar g(c_{\rm re}^2+c_{\rm im}^2)$] and mixed terms [$-gq_1c_{\rm im}$ and $-gq_1c_{\rm re}$]. These nonlinear terms are exclusively associated with the optical cavity and position q_1 of mechanical oscillator MR_1. However, altering the Coulomb coupling strength influences the momentum p_1 and p_2 of mechanical oscillators MR_1 and MR_2, which in turn affects their positions q_1 and q_2; ultimately, this will lead to a change in the motion state of the optical cavity. Conversely, nonlinear changes in the optical cavity influence the quadratic terms, leading to nonlinear behavior in the mechanical oscillator. From a mathematical standpoint, it can be demonstrated that variations in Coulomb coupling strength induce nonlinear effects on the mechanical oscillators and the optical cavity. Furthermore, the bifurcation diagrams in Figs. 9(i) and 9(s) clearly illustrate the system's transition from periodic motion to chaos. The $\rm LE_{max}$ in Figs. 9(j) and 9(t) further corroborate the onset of chaotic motion. These results underscore the influence of Coulomb coupling in amplifying the system's nonlinearity. A transition from period-doubling bifurcation to chaos occurs when the coupling strength surpasses a critical threshold.

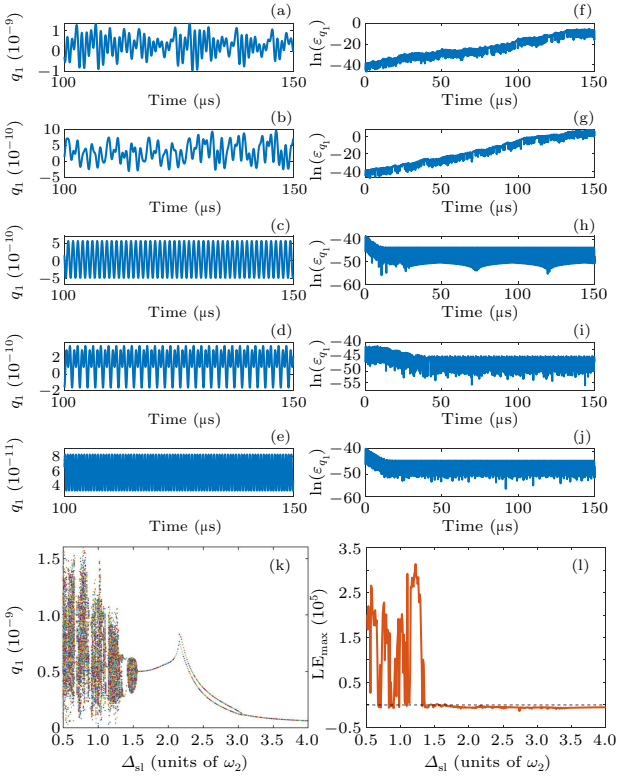


Fig. 10. (a)–(j) The evolution of position q_1 and its logarithmic perturbation $\ln(\varepsilon_{q_1})$ under the detuning $\Delta_{\rm sl}$ between the pump and probe fields. From top to bottom, the detuning $\Delta_{\rm sl}$ values are set to $0.6\omega_2$, $1.2\omega_2$, $2\omega_2$, $2.5\omega_2$ and $3.5\omega_2$. (k) Bifurcation diagram of the limit cycle amplitude as a function of detuning $\Delta_{\rm sl}$. (l) The maximum Lyapunov exponent $\rm LE_{max}$ of MR_1 as a function of detuning $\Delta_{\rm sl}$. Other parameters are identical to those in Fig. 7.

In addition to examining the influence of the probe field power $P_{\rm s}$ and Coulomb coupling strength λ on chaotic motion, figure 10 investigates the effect of detuning $\Delta_{\rm sl}$ between the pump and probe fields. As shown in Figs. 10(a) and 10(f), the evolution of position q_1 exhibits unpredictable complexity, and we observe the divergence of adjacent trajectories in the evolution of the logarithmic perturbation, confirming the onset of chaotic motion. In Figs. 10(b) and 10(g), as the detuning is further increased, oscillator MR_1 continues to display chaotic motion. However, at a certain detuning value $\Delta_{\rm sl} \geq 1.57\omega_2$ (shown in Fig. 10(c)), the evolution of position q_1 becomes regular and exhibits single-period harmonic motion, which can be described by a simple sine wave. This corresponds to evolution of the flat perturbation in Fig. 10(h), indicating that the mechanical oscillator is no longer sensitive to small changes in initial conditions and that adjacent trajectories do not diverge. Upon further increasing the detuning $3.06\omega_2 \geq \Delta_{\rm sl} \geq 2.16\omega_2$, as shown in Figs. 10(d) and 10(i), the system reaches a steady state and the evolution of logarithmic perturbation $\ln(\varepsilon_{q_1})$ exhibits the characteristic of period-doubling bifurcation. In Figs. 10(e) and 10(j), contrary to the common expectation, mechanical oscillator MR_1 does not transition from period-doubling to chaos, but instead returns to single-periodic motion. Bifurcation diagrams and maximum Lyapunov exponent curves corresponding to these conditions are shown in Figs. 10(k) and 10(l). These diagrams help identify the parameter range over which the mechanical oscillator exhibits periodic or chaotic motion as a result of detuning variation $\Delta_{\rm sl}$. Furthermore, after entering the period-doubling bifurcation, $\Delta_{\rm sl} \geq 2.16\omega_2$, continued increases in detuning $\Delta_{\rm sl}$ cause the amplitude of mechanical oscillator MR_1 to gradually decrease. These results suggest that increasing detuning $\Delta_{\rm sl}$ enhances the stability of the system, particularly when the probe frequency exceeds the pump frequency.

4. Conclusion

In this study, we theoretically examined the formation and control of optomechanical chaos in Coulomb interactions. Chaotic motion was observed under both single driving laser fields and bichromatic laser fields. Specifically, we also discovered tunable higher-order sidebands when driving a single laser field. In addition, beyond the influence of driving power and detuning, which induce the system's transition to a chaotic state, we discovered that increasing the Coulomb coupling strength enhances the cavity optomechanical nonlinearity. This amplification leads to period-doubling bifurcations, ultimately driving the system into chaos. Through numerical simulations, we identified the parameter range associated with chaotic behavior. Our findings offer a novel platform for the nonlinear study of cavity optomechanics and suggest a new route for the generation and control of chaos.

Acknowledgments

Project supported by Young Talents from Longyuan, Gansu Province (Liwei Liu), the Fundamental Research Funds

for the Central Universities, Northwest Minzu University (Grant No. 31920230134), Teaching Achievement Cultivation Project of Gansu Province Department of Education (Grant No. 2022GSJXCGPY-46), Special research topic on curriculum and teaching materials for primary, secondary and higher schools, Gansu Province Department of Education (Grant No. GSJC-Y2024204), and Quality improvement project for undergraduate talent training, Northwest Minzu University (Grant Nos. 2024YBJG-04 and 2024FCTD-03).

References

[1] Lemonde M A, Didier N and Clerk A A 2013 *Phys. Rev. Lett.* **111** 053602
[2] Zhang H, Eremeev V, Wu J, Orszag M and He B 2025 *Phys. Rev. E* **111** 014208
[3] Barzanjeh S, Xuereb A, Gröblacher S, Paternostro M, Regal C A and Weig E 2022 *Nat. Phys.* **18** 15
[4] Metzger C, Ludwig M, Neuenhahn C, Ortlied A, Favero I, Karrai K and Marquardt F 2008 *Phys. Rev. Lett.* **101** 133903
[5] Dong C, Zhang J, Fiore V and Wang H 2014 *Optica* **1** 425
[6] Xu X, Zhu H, Chen S and Zhang X 2024 *Opt. Express* **32** 7611
[7] Cao C, Mi S C, Gao Y P, He L Y, Yang D, Wang T J, Zhang R and Wang C 2016 *Sci. Rep.* **6** 22920
[8] Liu S, Yang W X, Shui T, Zhu Z and Chen A X 2017 *Sci. Rep.* **7** 17637
[9] Liu J H, Yu Y F, Wu Q, Wang J D and Zhang Z M 2021 *Opt. Express* **29** 12266
[10] Carmon T, Cross M C and Vahala K J 2007 *Phys. Rev. Lett.* **98** 167203
[11] Bakemeier L, Alvermann and Fehske H 2015 *Phys. Rev. Lett.* **114** 013601
[12] Zhang D W, You C and Lü X Y 2020 *Phys. Rev. A* **101** 053851
[13] Chen L T, Qin L G, Tian L J, Huang J H, Zhou N R and Gong S Q 2024 *Chin. Phys. B* **33** 064204
[14] Dong L H, Wu X J, Bai C H and Wu S X 2025 *Chin. Phys. B* **34** 020304
[15] Li H M, Yang B H, Yuan H C and Xu Y J 2023 *Chin. Phys. B* **32** 014202
[16] Elbert T, Ray W J, Kowalik Z J, Skinner J E, Graf K E and Birbaumer N 1994 *Physiological Reviews* **74** 1
[17] Kippenberg T J and Vahala K J 2007 *Opt. Express* **15** 17172
[18] Monifi F, Zhang J, Özdemir Ş K, Peng B, Bo F, Nori F and Yang L 2016 *Nat. Photon.* **10** 399
[19] Ma J, You C, Si L G., Xiong H, Li J, Yang X and Wu Y 2014 *Phys. Rev. A* **90** 043839
[20] Zhang D W, Zheng L L, Wang M and Zhou Y and Lü X Y 2024 *Phys. Rev. A* **109** 023529
[21] Ullah K, Jing H and Saif F 2018 *Phys. Rev. A* **97** 033812
[22] Sohail A, Ahmed R, Yu C S and Munir T 2020 *Phys. Scr.* **95** 035108
[23] Zhao Y N, Wang T, Wang D Y, Han X, Zhang S and Wang H F 2021 *Photonics* **8** 384
[24] Wang Q, Zhang J Q, Ma P C, Yao C M and Feng M 2015 *Phys. Rev. A* **91** 063827
[25] Wu Q, Zhang J Q, Wu J H, Feng M and Zhang Z M 2015 *Opt. Express* **23** 018534
[26] Náprstek J and Fischer C 2021 *Nonlinear Dyn.* **106** 1591
[27] Chapman R B and Plesset M S 1972 *J. Basic Eng.* **94** 142
[28] Kippenberg T J, Spillane S M and Vahala K J 2004 *Phys. Rev. Lett.* **93** 083904
[29] Rössler O E and Letellier C 2020 *Chaos in Toroidal Systems* (Cham: Springer) pp. 67–89
[30] Piergentili P, Natali R, Vitali D and Giuseppe G D 2022 *Photonics* **9** 99
[31] Piergentili P, Li W, Natali R, Malossi N, Vitali D and Giuseppe G D 2021 *New J. Phys.* **23** 073013
[32] Wang T, Han X, Liu S, Zhang S and Wang H F 2023 *Adv. Quantum Technol.* **6** 2200162
[33] Ma P C, Yan L L, Chen G B, Li X and Zhan Y B 2016 *Laser Phys. Lett.* **13** 125301
[34] Omari A 2019 *Chin. J. Phys.* **57** 435
[35] He Q, Badshah F, Din R U, Zhang H, Hu Y and Ge G Q 2018 *J. Opt. Soc. Am. B* **35** 1649
[36] Mekonnen H D, Tesfahannes T G, Darge T Y and Kumela A G 2023 *Sci. Rep.* **13** 13800
[37] Yan X B 2021 *J. Phys. B: Atom. Mol. Opt. Phys.* **54** 035401
[38] Yan X B 2020 *Phys. Rev. A* **101** 043820
[39] Linsay P S 1981 *Phys. Rev. Lett.* **47** 1349
[40] Awal N M and Epstein I R 2021 *Phys. Rev. E* **104** 024211
[41] Kantz H 1994 *Phys. Lett. A* **185** 77
[42] Pechuk V D, Krasnopolskaya T S and Pechuk E D 2022 *Maximum lyapunov exponent calculation* (Cham: Springer) pp. 327–335
[43] Ma P C, Zhang J Q, Xiao Y, Feng M and Zhang Z M 2014 *Phys. Rev. A* **90** 043825
[44] Tian L and Zoller P 2004 *Phys. Rev. Lett.* **93** 266403
[45] Xia C C, Yan X B, Tian X D and Gao F 2019 *Opt. Commun.* **451** 197
[46] Tanaka T 1998 *Advances in Neural Information Processing Systems* **11** 351
[47] Aspelmeyer M, Kippenberg T J and Marquardt F 2014 *Rev. Mod. Phys.* **86** 1391
[48] Skokos C 2010 *The Lyapunov Characteristic Exponents and Their Computation* (Berlin: Springer) pp. 63–135
[49] Lü X Y, Jing H, Ma J Y and Wu Y 2015 *Phys. Rev. Lett.* **114** 253601
[50] Bai T R, Chen Z D, Zhang J Q, Yan D, He Z W, Zhang S, Zhao J and Yu Y 2023 *Phys. Rev. A* **107** 033522